

Compact scanning confocal chromatic sensor enabling precision 3-D measurements

DANIEL WERTJANZ^{1,2,*}, THOMAS KERN^{1,2}, ERNST CSENSICS¹, GERHARD STADLER¹, AND GEORG SCHITTER¹

¹Christian Doppler Laboratory for Precision Engineering for Automated In-Line Metrology, Automation and Control Institute (ACIN), Technische Universität Wien, 1040 Vienna, Austria

²These authors contributed equally.

*Corresponding author: wertjanz@acin.tuwien.ac.at

Compiled August 16, 2021

This paper proposes a compact and lightweight scanning confocal chromatic sensor (SCCS) for robot-based precision 3-D surface measurement applications. The integrated system design includes a 2-D fast steering mirror (FSM) to manipulate the optical path of a high precision 1-D confocal chromatic sensor (CCS). A data-driven calibration procedure is used to accurately combine the FSM deflection angles and the correspondingly measured distances to the sample surface in order to obtain a correctly reconstructed 3-D image. Lissajous scan trajectories are applied to enable efficient scans of the sample surface. The SCCS provides 3-D images at frame rates of up to 1 fps and a measurement volume of $0.35 \times 0.25 \times 1.8 \text{ mm}^3$, as well as the measurement of arbitrary regions of interest. Using a calibration standard including structures with defined sizes, the lateral and axial resolution is determined to 2.5 μm and 76 nm, respectively. © 2021 Optical Society of America

<http://dx.doi.org/10.1364/ao.XX.XXXXXX>

1. INTRODUCTION

Modern high-tech industrial manufacturing systems show a continuously growing demand for precision and throughput [1]. Inline measurements can provide real-time quality control [2] of produced goods and are considered a key factor for future industrial production [3], enabling realtime optimization of the manufacturing process and production parameter settings [4, 5]. Since surface condition and shape are often features of interest or quality indicators of machined goods, (inline) 3-D measurements have become increasingly important in recent years [6–9]. To provide the flexibility of measuring in arbitrary orientations and locations, such as needed for freeform-shaped goods [10], industrial robots can be employed to align the measurement tool to the sample surface [11].

However, the limited accuracy of industrial robots [12] and the vibrations in an industrial environment are corrupting 3-D measurements on the single-micrometer scale by causing motion blur [13]. To enable robot-based precision measurements on freeform surfaces, a MAGLEV tracking module with arbitrary operation orientation has been proposed recently [14]. The tracking module can be mounted to a robot arm and generates a contactless stiff link between the measurement tool on the tracking platform and the sample surface via feedback control, establishing lab conditions directly in a vibration-prone environment.

High precision 3-D measurement tools, such as atomic force

microscopes or coordinate measurement machines with optical sensors, can provide nanometer resolution [15, 16] but are typically rather bulky and therefore not suited for the targeted robot-based application. In a recent approach, a confocal chromatic sensor (CCS) with a rotationally actuated lens stack has been used to obtain a compact 3-D measurement tool with a lateral resolution of about 25 μm [17]. Another way to obtain precision 3-D measurements with high frame rates is to manipulate only the optical path of a fast 1-D displacement sensor using galvanometer scanners [18] or fast steering mirrors (FSMs) [19]. Triangulation or confocal chromatic sensors are typically used in such opto-mechatronic measurement systems [20–23], as they achieve resolutions down to tens of nanometers and have reasonably large measurement ranges [17, 24]. The high acceptance angle of several tenths of degrees and the high material independency [25] make CCSs particularly interesting when targeting freeform-shaped surfaces with various material properties. However, a compact 3-D measurement tool, which combines the high axial resolution of a CCS with the high scanning speed of an FSM, is still not available.

The contribution of this paper is the integrated design and experimental validation of a compact FSM-based scanning confocal chromatic sensor (SCCS), suitable for mounting on a tracking platform and enabling high performance 3-D measurements for robot-based applications.

The remaining paper is organized as follows. Section 2 presents the system concept and integrated design of the SCCS. Following the system modeling and simulation results in Section 3, the implementation of the individual system components is discussed in Section 4. The proposed data-driven calibration procedure of the SCCS is presented in Section 5 and Section 6 experimentally evaluates the achieved 3-D imaging performance. Finally, Section 7 concludes the paper.

2. COMPACT FSM-BASED SCCS CONCEPT

A. System requirements

Considering the targeted application of vibration-compensated robot-based precision inline measurements on freeform surfaces, a compact and lightweight design of the optical 3-D measurement tool is required, which is tailored for a measurement platform [14]. The electromagnetically actuated and freely floating platform allows a total mass of about 300 g for the 3-D measurement tool to still achieve a sufficiently high tracking control bandwidth. A lateral measuring range of at least $250 \times 250 \mu\text{m}^2$ is desirable, which is about one order of magnitude larger than the positioning accuracy of an industrial robot [12]. In the targeted robot-based application, the measuring range of the 3-D measurement tool will be extended by moving the robot arm and using image stitching techniques [26]. Chromatic confocal sensors typically show spot diameters in the single-micrometer range and sub-micrometer axial resolution [27]. Considering these values, sub- and single-micrometer resolution in the axial and lateral direction, respectively, are targeted for the SCCS. An imaging rate of 1 frame per second (fps) is desired in order to enable a reasonable throughput for applications in industrial production lines. The targeted specifications of the compact SCCS system are summarized in Tab. 1.

Table 1. System requirements of the 3-D measurement tool.

Property	Value
Mass	< 300 g
Lateral measurement range	$250 \times 250 \mu\text{m}^2$
Axial resolution	< 1 μm
Lateral resolution	< 10 μm
Imaging rate	up to 1 fps

B. System design

The integrated design of the SCCS is presented in Fig. 1a and includes a high precision CCS and a pre-existing compact high performance FSM [28]. The FSM is actuated by a hybrid-reluctance actuator and provides an integrated eddy current sensor system to determine the actual mirror position. Moreover, it is compact with a diameter of 32 mm and lightweight with a mass of about 130 g. A detailed description of the integrated FSM can be found in [28]. Precise alignment between the FSM and the CCS is ensured by a stiff alignment frame. Since the achievable lateral measurement range strongly depends on the length of the deflected light beam, the CCS is placed as close as possible to the FSM. The FSM is tilted by -45° around the y_0 -axis with respect to the CCS, resulting in an optical beam deflection in

z_0 -direction, assuming the FSM being in its center position. By actuating the tip (ϕ) and tilt (θ) axis of the FSM, the measuring spot is scanned over the sample and 3-D measurements of the surface topography are enabled. To transform the positions of the surface measured by the internal sensors of the FSM and the related displacement values measured by the CCS into a 3-D image, a calibration procedure is used, which is shown in detail in Section 5.

3. SYSTEM MODELING

Considering the CCS and FSM arrangement shown in Fig. 1b, the parameters to achieve the targeted measurement range listed in Tab. 1 need to be determined in a first step. Therefore, the measuring spot position on the sample surface is required to be modelled as a function of the FSM deflection. Two coordinate systems are introduced for the sake of convenience; the inertial coordinate system (COS_0) $[x_0, y_0, z_0]^T$ is placed in the pivot point of the FSM, while the second mirror-fixed coordinate system (COS_1) $[x_1, y_1, z_1]^T$ is situated in the center of the mirror surface, with h_{FSM} being the distance between the pivot and the mirror surface (see Fig. 1b). Hereinafter, all vectors which are described in COS_0 or COS_1 are marked with the indices 0 and 1, respectively. Using the tip (ϕ) and tilt angles (θ), the coordinate transformation from COS_1 to COS_0 can be described with a rotary component \mathbf{R}_0^1 and a translatory component \mathbf{d}_0^1 given by

$$\mathbf{R}_0^1 = \mathbf{R}_{y, -\frac{\pi}{4} + \phi} \mathbf{R}_{x, \theta} = \begin{bmatrix} s_{\frac{\pi}{4} + \phi} & 0 & -c_{\frac{\pi}{4} + \phi} \\ 0 & 1 & 0 \\ c_{\frac{\pi}{4} + \phi} & 0 & s_{\frac{\pi}{4} + \phi} \end{bmatrix} \begin{bmatrix} 1 & 0 & 0 \\ 0 & c_\theta & -s_\theta \\ 0 & s_\theta & c_\theta \end{bmatrix} \quad (1a)$$

$$\mathbf{d}_0^1 = \begin{bmatrix} -c_{\frac{\pi}{4} + \phi} c_\theta h_{\text{FSM}} \\ -s_\theta h_{\text{FSM}} \\ s_{\frac{\pi}{4} + \phi} c_\theta h_{\text{FSM}} \end{bmatrix}, \quad (1b)$$

with $s_i = \sin(i)$ and $c_i = \cos(i)$. Combining Eq. (1a) and Eq. (1b) yields to the homogeneous transformation matrix

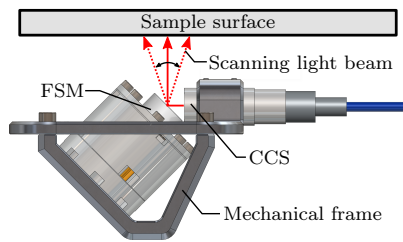
$$\mathbf{H}_0^1 = \begin{bmatrix} s_{\frac{\pi}{4} + \phi} & -c_{\frac{\pi}{4} + \phi} s_\theta & -c_{\frac{\pi}{4} + \phi} c_\theta & -c_{\frac{\pi}{4} + \phi} c_\theta h_{\text{FSM}} \\ 0 & c_\theta & -s_\theta & -s_\theta h_{\text{FSM}} \\ c_{\frac{\pi}{4} + \phi} & s_{\frac{\pi}{4} + \phi} s_\theta & s_{\frac{\pi}{4} + \phi} c_\theta & s_{\frac{\pi}{4} + \phi} c_\theta h_{\text{FSM}} \\ 0 & 0 & 0 & 1 \end{bmatrix}, \quad (2)$$

which is used to transform a point $[\mathbf{P}_0 \ 1]^T = \mathbf{H}_0^1 [\mathbf{P}_1 \ 1]^T$ from COS_1 into COS_0 . Note that the 4th row in Eq. (2) is required to obtain full rank and invertibility.

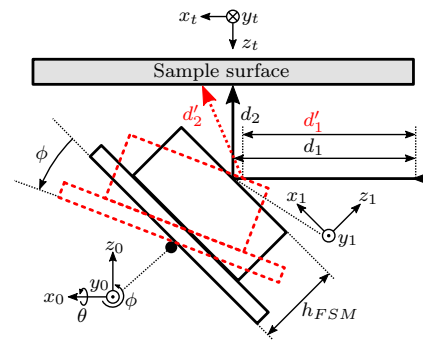
With the mirror in its center position, the incoming and the deflected beam $\mathbf{k}_{\text{inc}1}$ and $\mathbf{k}_{\text{def}1}$, respectively, differ only in the sign of their z_1 -component. Hence, the direction of the deflected beam

$$\mathbf{k}_{\text{def}0} = \mathbf{R}_0^1 \left(\mathbf{z}_{\text{inv}} \left(\mathbf{R}_1^0 \mathbf{k}_{\text{inc}0} \right) \right) \quad (3)$$

is obtained as a function of the tip (ϕ) and tilt (θ) angles of the FSM by transforming the incoming beam $\mathbf{k}_{\text{inc}1}$ into COS_1 using the relation $\mathbf{R}_1^0 = (\mathbf{R}_0^1)^{-1}$, multiplying the transformed vector by



(a) FSM-based scanning confocal chromatic sensor CAD design.



(b) Schematic illustration of the scanning operation.

Fig. 1. System design. (a) depicts the CAD design of the FSM-based SCCS. (b) illustrates the geometry of the scanning motion and the beam deflection. The FSM neutral position with the resulting beam deflection is shown in solid black, while the tilted FSM and the resulting deflection beam is indicated in dashed red.

$$\mathbf{z}_{\text{inv}} = \begin{bmatrix} 1 & 0 & 0 \\ 0 & 1 & 0 \\ 0 & 0 & -1 \end{bmatrix} \quad (4)$$

and transforming the resulting vector back into COS_0 . The position of the light spot on the mirror surface can be written as

$$\begin{bmatrix} \mathbf{P}_{\text{spot,FSM}_1} \\ 1 \end{bmatrix} = \mathbf{H}_1^0 \begin{bmatrix} \mathbf{P}_{\text{CCS}_0} + d_1 \mathbf{k}_{\text{inc}_0} \\ 1 \end{bmatrix}, \quad (5)$$

with $\mathbf{P}_{\text{CCS}_0}$ being the position of the CCS lense in COS_0 . Since the rotation and reflexion point in the system design do not coincide (see Fig. 1b), a translatory component of the FSM movement occurs, resulting in a varying distance d_1 between the CCS and the mirror surface. Solving the z_1 component $P_{\text{spot,FSM},z_1} = 0$ for d_1 yields the location of the spot on the mirror surface given by $\mathbf{P}_{\text{spot,FSM}_0} = \mathbf{f}_1(\phi, \theta)$, which is a function of ϕ and θ .

In a similar way, the distance from the spot on the mirror surface to the sample surface d_2 can be obtained. Furthermore, the spot location on the sample surface is given by

$$\begin{bmatrix} x_t \\ y_t \\ z_t \end{bmatrix} = \mathbf{f}_2(\phi, \theta). \quad (6)$$

Note that the analytical expressions of \mathbf{f}_1 and \mathbf{f}_2 are extensive and therefore not shown. The actual sample height can be written as $z_t = d_1 + d_2 - (d_{1,0} + d_{2,0}) = d - d_0$, with the measured distance d_0 for the FSM being in its center position.

Assuming a flat surface in the $x_t y_t$ -plane as well as the parameter values $d_{1,0} = 5$ mm and $d_{2,0} = 10$ mm and a perfectly aligned system, the evaluation of Eq. (6) for an FSM actuation range of $\pm 1^\circ$ in both axes leads to an effective scan area of 0.56×0.39 mm². The maximum scanner bow is about 2.8 μm , which requires system calibration, discussed in Section 5, to compensate for it.

4. SYSTEM IMPLEMENTATION

Based on the modeling results, appropriate system components are chosen for implementation. An image of the fully integrated SCCS is shown in Fig. 2 and the individual components are described in detail in the following. The implemented SCCS is about $75 \times 63 \times 55$ mm³ in size and has a total mass of about 300 g, which is well within the targeted mass specification in Tab. 1.

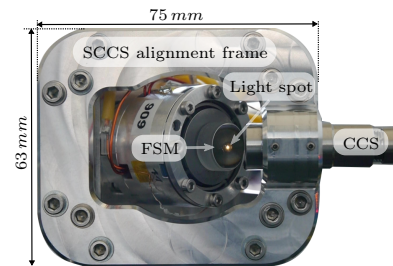


Fig. 2. Image of the implemented SCCS with the light spot of the CCS clearly visible on the FSM.

A. CCS

The compact CCS head IFS2404-2 and the controller IFC2471 LED (Micro-Epsilon, Ortenburg, Germany) are chosen to enable displacement measurements with 40 nm axial resolution at a maximum measurement rate of 70 kHz [27]. The sensor head is 12 mm in diameter and 42 mm in length, provides a measurement range of 2 mm starting at a distance of 14 mm, and a light spot diameter of 10 μm . The CCS is arranged in a distance of $d_{1,0} = 5$ mm (see Fig. 1b) to the mirror's center. This yields a deflected light beam length of $d_{2,0} = 10$ mm for the FSM in its center position and the sample surface placed in the CCS' mid-range. In order to place the start of the axial measuring range beyond the upper edge of the FSM housing, a rather thick mirror (PF0503, Thorlabs, USA) with a height of 6 mm and a diameter of 12.7 mm is integrated. As a result, the CCS's measuring range starts about 1 mm beyond the upper edge of the FSM housing.

B. FSM

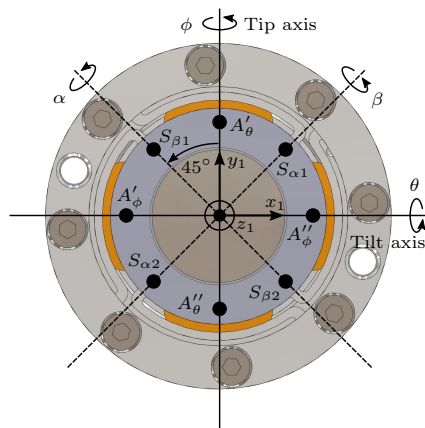


Fig. 3. Top-view of the FSM CAD model with 45° rotated actuation and sensor axes [28].

Considering the system requirements in Tab. 1, a compact FSM with large scan range [28] is selected. The FSM is 30 mm in height and has a diameter of 32 mm. Based on the hybrid-reluctance actuation principle, it provides an actuation range of up to $\pm 3^\circ$. The deflections α and β are obtained from the differential signals of the integrated eddy current sensors ($S_{\alpha 1}, S_{\alpha 2}$) and ($S_{\beta 1}, S_{\beta 2}$). As indicated in Fig. 3, the sensor axes are rotated by 45° with respect to the actuation axes. Therefore, the transformation

$$\begin{bmatrix} \phi \\ \theta \end{bmatrix} = \begin{bmatrix} \frac{\sqrt{2}}{2} & \frac{\sqrt{2}}{2} \\ -\frac{\sqrt{2}}{2} & \frac{\sqrt{2}}{2} \end{bmatrix} \begin{bmatrix} \alpha \\ \beta \end{bmatrix} \quad (7)$$

is used to calculate the position of the tip (ϕ) and tilt (θ) axis in the actuator space.

C. SCCS alignment frame

Good alignment of the CCS with respect to the FSM is ensured by design and low manufacturing tolerances of the SCCS alignment frame, as illustrated in Fig. 2. Since a stiff and lightweight design is desired, aluminum is chosen as material. Moreover, it provides mounting holes for the future operation on a vibration-compensating measurement platform [14].

5. DATA-DRIVEN SYSTEM CALIBRATION

As discussed in Section 3, mounting tolerances of the FSM and CCS can cause misalignment, resulting in variations of the measurement area and scanner bow. Figure 4a exemplarily shows the simulation results of a misaligned CCS with the direction of the incoming light beam $\mathbf{k}_{\text{inc}} = \frac{1}{\sqrt{1+2 \cdot 0.05^2}} [1 \ 0.05 \ 0.05]^T$ and an FSM scanning amplitude of 1° in both axes. The lateral scan range appears skewed and twisted as well as the whole surface is tilted in z -direction. Additionally, the entire scan range is offset by 455 μm in x -direction and 563 μm in y -direction.

To compensate for any system misalignment, a data-driven approach using a CMOS camera (DMM 37UX273-ML, The Imaging Source, Bremen, Germany) is chosen to calibrate the SCCS. The camera is placed in axial mid-range of the CCS with the

FSM in its center position. Using the camera's pixel size of 3.45 μm , the measurement range is obtained by recording the lateral movement of the light spot on the camera sensor for various deflection angles ϕ, θ of the FSM and the corresponding measured displacement of the CCS (see Fig. 4b). A shutter time of 1 μs is chosen to prevent the CMOS sensor from saturation. Similar effects as in the previously discussed simulation can be observed. The deviation in z -direction is about 20 μm and the lateral scan range appears skewed and twisted. Note that the lateral measurement range offset is not relevant for the targeted 3-D measurements and cannot be evaluated using a flat surface. The corner of the measured lateral scan range on the bottom left is set to $(x = 0/y = 0)$.

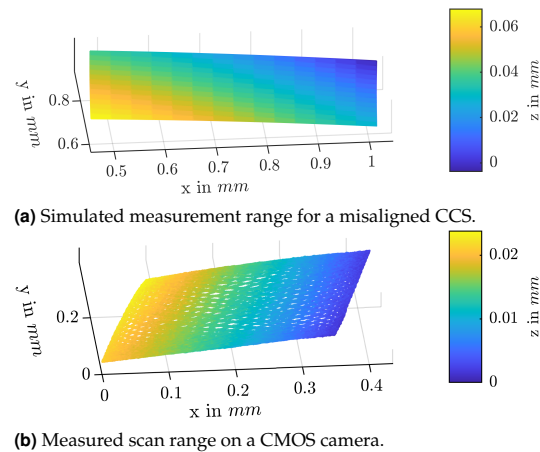


Fig. 4. Impact of a misaligned system on the measurement range. In (a) the simulation results for a slightly tilted CCS and incoming light beam are shown. (b) depicts the measured image on a CMOS camera placed in the middle of the CCS' axial measurement range.

Using the measured data in Fig. 4b and the corresponding tip and tilt angles of the FSM, 5th-order polynomial surfaces $f_x(\phi, \theta)$ and $f_y(\phi, \theta)$ are fitted for both lateral degrees of freedom x and y . To correct the measured sample height z by the known scanner bow, a 3rd-order polynomial surface $f_z(\phi, \theta)$ is fitted and subtracted from the measured sample height $d - d_0$. For a measured surface data set $\{\phi, \theta, d\}$, the image reconstruction procedure

$$x = f_x(\phi, \theta) \quad (8a)$$

$$y = f_y(\phi, \theta) \quad (8b)$$

$$z = d - d_0 - f_z(\phi, \theta) \quad (8c)$$

is used to obtain the targeted three-dimensional point cloud of the sample surface. The coefficients of each fitted polynomial surface

$$\begin{aligned} f_i(\phi, \theta) = & p_{00} + p_{10}\phi + p_{01}\theta + p_{20}\phi^2 + p_{11}\phi\theta + p_{02}\theta^2 + \\ & p_{30}\phi^3 + p_{21}\phi^2\theta + p_{12}\phi\theta^2 + p_{03}\theta^3 + p_{40}\phi^4 + p_{31}\phi^3\theta + \\ & p_{22}\phi^2\theta^2 + p_{13}\phi\theta^3 + p_{04}\theta^4 + p_{50}\phi^5 + p_{41}\phi^4\theta + p_{32}\phi^3\theta^2 + \\ & p_{23}\phi^2\theta^3 + p_{14}\phi\theta^4 + p_{05}\theta^5, \quad i = \{x, y, z\} \quad (9) \end{aligned}$$

are listed in Tab. 2.

Table 2. Coefficients of the fitted surfaces used for the 3-D image reconstruction.

Coeff.	$f_x(\phi, \theta)$	$f_y(\phi, \theta)$	$f_z(\phi, \theta)$
p_{00}	566.9 μm	164.4 μm	985.1 μm
p_{10}	-18.3 $\mu\text{m}/\text{V}$	-66.7 $\mu\text{m}/\text{V}$	253 nm/V
p_{01}	-4.7 $\mu\text{m}/\text{V}$	-16.2 $\mu\text{m}/\text{V}$	-52.5 nm/V
p_{20}	-441.7 nm/V^2	-71.8 nm/V^2	119.6 nm/V^2
p_{11}	-313.4 nm/V^2	236.9 nm/V^2	104.1 nm/V^2
p_{02}	-518.8 nm/V^2	-31 nm/V^2	48.2 nm/V^2
p_{30}	-41.5 nm/V^3	-26.4 nm/V^3	11.2 nm/V^3
p_{21}	-264.1 nm/V^3	253.7 nm/V^3	-3.5 nm/V^3
p_{12}	-163.4 nm/V^3	35.4 nm/V^3	19.3 nm/V^3
p_{03}	-25.4 nm/V^3	-87.6 nm/V^3	-1.1 nm/V^3
p_{40}	32.9 nm/V^4	29.4 nm/V^4	0
p_{31}	49 nm/V^4	-45.6 nm/V^4	0
p_{22}	26.8 nm/V^4	-1.3 nm/V^4	0
p_{13}	57.7 nm/V^4	-48.1 nm/V^4	0
p_{04}	40.9 nm/V^4	23.8 nm/V^4	0
p_{50}	1.2 nm/V^5	5 nm/V^5	0
p_{41}	25.4 nm/V^5	-32.3 nm/V^5	0
p_{32}	14.6 nm/V^5	-5 nm/V^5	0
p_{23}	17.1 nm/V^5	-12.7 nm/V^5	0
p_{14}	1.9 nm/V^5	4.4 nm/V^5	0
p_{05}	1.3 nm/V^5	5.48 nm/V^5	0

6. EVALUATION OF SYSTEM PERFORMANCE

In a first step, the lateral measurement range of the SCCS is determined. As modelled in Section 3 and shown in Fig. 4b, a scanning amplitude of about 1° in both axes is required to obtain a lateral measurement range of $0.35 \times 0.25 \text{ mm}^2$, which exceeds the targeted specification in Tab. 1. Considering the CCS' axial measurement range of 2 mm and the measured scanner bow, sample structures with heights of up to $\pm 0.9 \text{ mm}$ around the mid-range can be measured.

Lissajous scan trajectories are chosen for the FSM in order to obtain efficient and dense 3-D measurements [29]. In the following, f_{tip} and f_{tilt} denote the scanning frequency of the tip and tilt axis, respectively. The total measurement time T is set to be equivalent to the period duration of the Lissajous trajectory. Thus, the same trajectory is performed for each scan, solely the scan speed is varied by the measurement time T . For a tip axis driving frequency of $f_{\text{tip}} = 57 \text{ Hz}$, a driving frequency $f_{\text{tilt}} = 43 \text{ Hz}$ on the tilt axis is an appropriate value to achieve both, a dense Lissajous trajectory and the desired imaging rate of $\frac{1}{T} = 1 \text{ fps}$ [29]. By increasing the measurement time T and applying smoothing filters to the measured data, e.g. moving averaging, 3-D images with higher resolution can be obtained.

A. Calibration-based image reconstruction

In a next step, the image reconstruction procedure from Eq. (8) is demonstrated on a silicon reference grid (Nanuler Calibration Standard, Applied NanoStructures Inc., Mountain view, CA, USA) with $20 \mu\text{m}$ pitch and step heights of $25 \mu\text{m}$. Figure 5a shows the measured raw data for the aforementioned Lissajous trajectory and a measurement time of $T = 30 \text{ s}$. On average, the grating pitch along the cross section at $\theta = 0 \text{ V}$ in the raw data is $\bar{\Lambda}_r = 0.31 \text{ V}$ with a standard deviation of $\sigma_r = 4.7\% \cdot \bar{\Lambda}_r$. In order to transform the FSM deflection angles (in V) and the corresponding distances to the sample surface into a correctly reconstructed 3-D image, the reconstruction procedure from Eq. (8) is used. The result is normalized by subtracting a fitted plane and the obtained 3-D image is shown in Fig. 5b. Although the aspect ratio of the grating is too low to measure the correct height due to the gap width equalling the CCS' spot diameter, a mean grating pitch of $\bar{\Lambda}_c = 20.37 \mu\text{m}$ and standard deviation of $\sigma_c = 3.3\% \cdot \bar{\Lambda}_c$ are obtained in the resulting 3-D image along the cross section at $y = 150 \mu\text{m}$. The standard deviation in percent of the mean value is lower than in the raw data image, indicating that the 3-D image resulting from the calibration-based reconstruction is less distorted.

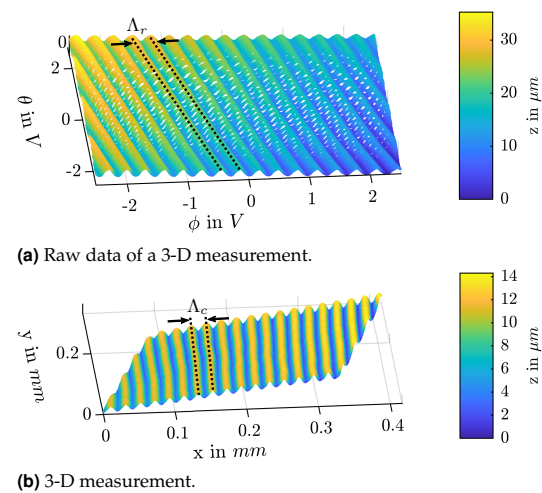


Fig. 5. Raw data and reconstructed image using the imaged reconstruction procedure from Eq. (8). Λ_r and Λ_c represent the measured pitch in the raw and reconstructed image, respectively.

B. Fast 3-D surface measurements

To achieve the targeted imaging rate of 1 fps, specified in Tab. 1, a total measurement time of $T = 1 \text{ s}$ is applied. Figure 6 shows the results for the fast 3-D imaging on the same grating as used in Fig. 5. Due to the shorter measurement time, less data points are measured. However, the grating is still clearly visible in the 3-D image. Thus, the SCCS is capable of providing a fast overview measurement mode to identify a potential region of interest (ROI).

C. High resolution 3-D surface measurements

The axial and lateral resolution of the SCCS are evaluated using a calibration standard (HS-500MG, BudgetSensors, Sofia, Bulgaria), which provides silicon sample structures with a defined

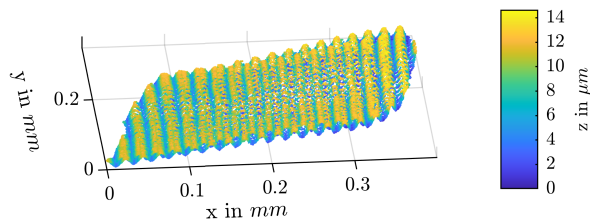
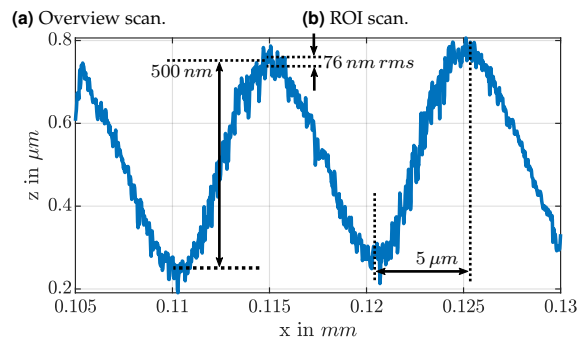
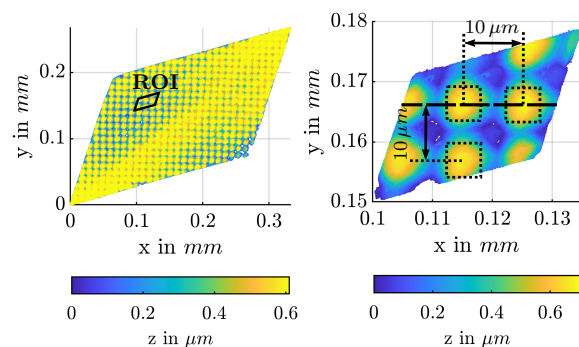


Fig. 6. Measurement results for fast 3-D imaging. The grating with 20 μm pitch is clearly visible for a fast scan with 1 fps.

height of 500 nm and pitches of 5 and 10 μm . Using the same scan trajectory as described in the previous subsection, Fig. 7a shows a 30 s-overview scan on the square pillars structure area with 10 μm pitch.



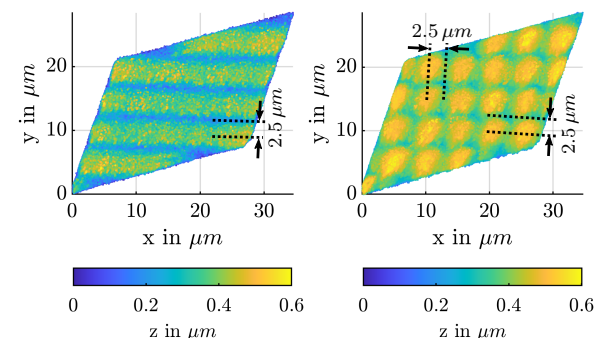
(c) Cross section in ROI at $y = 0.167$ mm.

Fig. 7. 3-D measurement results on a square pillars structure with 10 μm pitch. a) shows an overview image. b) presents the measured ROI from a) which is in good accordance with sample definition. In c) the cross section at $y = 0.167$ mm in the ROI from b) (dashed black) is plotted, with the structure height of 500 nm clearly visible.

The measurement data is smoothed using a moving average filter with a window length $N = 16$. To enable high resolution measurements of particular regions of interest (ROIs), a high resolution scan with reduced scanning amplitude and extended measurement time can be performed. The ROI indicated in Fig. 7a is selected and measured ($T = 120$ s, $N = 16$) with the results shown in Fig. 7b. Due to measurement and filtering blur, the square pillars appear circular. Nevertheless, the measured structure pitch of 10 μm still matches the sample def-

inition. Fig. 7c shows the corresponding cross section plot at $y = 0.167$ mm. The sample height of 500 nm is measured accurately. On top of a square pillar, the measurement noise is about 76 nm rms, which can be regarded as the minimum axial resolution of the SCCS and is in accordance with the values given in [27].

Finally, the lateral resolution of the SCCS is evaluated on the 5 μm pitch structures. Figure 8 depicts the measured 3-D images of the grating and circular pillar structure for $T = 120$ s and $N = 16$. In both images, the height of 300 nm measured by the SCCS differs from the sample definition, because of the light spot diameter being four times bigger than the sample structures and therefore the aspect ratio being too low. However, in the lateral axes, the individual structures are still distinguishable which demonstrates a lateral resolution of at least 2.5 μm .



(a) 5 μm pitch grating. **(b)** 5 μm pitch circular pillars.

Fig. 8. Measurement result on a) 5 μm pitch grating and b) a 5 μm pitch circular pillars structure. A lateral resolution of 2.5 μm is achieved.

In summary, the compact and lightweight SCCS provides a fast measurement mode with an imaging rate of 1 fps and is capable of measuring 3-D surfaces with 2.5 μm lateral and 76 nm axial resolution.

7. CONCLUSION

In this paper, a compact and lightweight scanning confocal chromatic sensor (SCCS) is designed, implemented and experimentally evaluated. Based on a high performance fast steering mirror (FSM) and a high precision confocal chromatic sensor (CCS), precision 3-D measurements for future robot-based freeform surface measurement applications are enabled. The entire system is about $75 \times 63 \times 55 \text{ mm}^3$ in size and has a total mass of about 300 g. A data-driven calibration procedure is implemented to transform the deflection angles of the FSM and the corresponding distance to the sample surface measured by the CCS into a 3-D image of the surface structure. For a sample surface placed in the axial mid-range of the CCS, the achieved measurement volume is about $0.35 \times 0.25 \times 1.8 \text{ mm}^3$. Based on a Lissajous scan trajectory, the SCCS is capable of performing fast 3-D measurements with an imaging rate of 1 fps. Experimental results show an lateral and axial resolution of about 2.5 μm and 76 nm, respectively. Future work includes the integration of the SCCS on a magnetically levitated vibration-compensating measurement platform acting as a robot end-effector to enable high resolution inline 3-D measurements.

Funding. Christian Doppler Forschungsgesellschaft; Bundesministerium für Digitalisierung und Wirtschaftsstandort; Österreichische Nationalstiftung für Forschung, Technologie und Entwicklung; MICRO-EPSILON MESSTECHNIK GmbH & Co. KG; ATENSOR Engineering and Technology Systems GmbH.

Disclosures. The authors declare no conflicts of interest.

Data availability. Data underlying the results presented in this paper are not publicly available at this time but may be obtained from the authors upon reasonable request.

REFERENCES

1. T. Uhrmann, T. Matthias, M. Wimplinger, J. Burggraf, D. Burgstaller, H. Wiesbauer, and P. Lindner, "Recent progress in thin wafer processing," in *2013 IEEE International 3D Systems Integration Conference (3DIC)*, (2013), pp. 1–8.
2. R. Schmitt and F. Moenning, "Ensure success with inline-metrology," in *XVIII IMEKO World Congress - Metrology for a Sustainable Development*, (2006).
3. D. Imkamp, R. Schmitt, and J. Berthold, "Blick in die Zukunft der Fertigungsmesstechnik - Die VDI/VDE-GMA Roadmap Fertigungsmesstechnik 2020." *Tech. Messen* **10(79)**, 433–439 (2012).
4. W. Gao, H. Haitjema, F. Fang, R. Leach, C. Cheung, E. Savio, and J. Linares, "On-machine and in-process surface metrology for precision manufacturing," *CIRP Annals* **68**, 843 – 866 (2019).
5. M. Grasso and B. Colosimo, "Process defects and in situ monitoring methods in metal powder bed fusion: a review," *Meas. Sci. Technol.* **28**, 044005 (2017).
6. A. Yogeswaran and P. Payeur, "3d surface analysis for automated detection of deformations on automotive body panels," in *New Advances in Vehicular Technology and Automotive Engineering*, (IntechOpen, 2012).
7. T.-F. Yao, A. Duenner, and M. Cullinan, "In-line dimensional metrology in nanomanufacturing systems enabled by a passive semiconductor wafer alignment mechanism," *J. Micro- Nano-Manufacturing* **5(1)** (2016).
8. H. Schwenke, U. Neuschaefer-Rube, T. Pfeifer, and H. Kunzmann, "Optical methods for dimensional metrology in production engineering," *CIRP Annals* **51(2)**, 685 – 699 (2002).
9. G. Sansoni, M. Trebeschi, and F. Docchio, "State-of-the-art and applications of 3d imaging sensors in industry, cultural heritage, medicine, and criminal investigation," *Sensors (Basel, Switzerland)* **9**, 568–601 (2009).
10. E. Savio, L. D. Chiffre, and R. Schmitt, "Metrology of freeform shaped parts," *CIRP Annals* **56**, 810 – 835 (2007).
11. J. Rejc, J. Cinkelj, and M. Munič, "Dimensional measurements of a gray-iron object using a robot and a laser displacement sensor," *Robotics Comput. Manuf.* **25(1)**, 155–167 (2009).
12. U. Schneider, J. R. D. Posada, M. Drust, and A. Verl, "Position control of an industrial robot using an optical measurement system for machining purposes," *Proc. 11th Int. Conf. on Manuf. Res. (ICMR2013)*, Cranfield, UK (2013).
13. R. Saathof, M. Thier, R. Hainisch, and G. Schitter, "Integrated system and control design of a one dof nano-metrology platform," *Mechatronics* **47**, 88 – 96 (2017).
14. D. Wertjanz, E. Csencsics, and G. Schitter, "3 dof vibration compensation platform for robot-based precision inline measurements on free-form surfaces," *IEEE Transactions on Ind. Electron. (Early Access)* (2021).
15. R. Leach, *Fundamental Principles of Engineering Nanometrology* (Elsevier, 2014), 2nd ed.
16. R. Henselmans, L. Cacace, G. Kramer, P. Rosielle, and M. Steinbuch, "The nanomefos non-contact measurement machine for freeform optics," *Precis. Eng.* **35**, 607–624 (2011).
17. M. E. Fuerst, E. Csencsics, C. Haider, and G. Schitter, "Confocal chromatic sensor with an actively tilted lens for 3d measurement," *J. Opt. Soc. Am. A* **37**, B46–B52 (2020).
18. C. Yu, X. Chen, and J. Xi, "Modeling and calibration of a novel one-mirror galvanometric laser scanner," *Sensors* **17** (2017).
19. E. Csencsics, S. Ito, J. Schlarp, and G. Schitter, "System integration and control for 3d scanning laser metrology," *IEEE J. Ind. Appl.* **8** (2019). Invited.
20. S. Ito, M. Poik, E. Csencsics, J. Schlarp, and G. Schitter, "High-speed scanning chromatic confocal sensor for 3-d imaging with modeling-free learning control," *Appl. Opt.* **59**, 9234–9242 (2020).
21. B. Chun, K. Kim, and D. Gweon, "Three-dimensional surface profile measurement using a beam scanning chromatic confocal microscope." *The Rev. scientific instruments* **80**, 073706 (2009).
22. T. Kim, S. Kim, D. Do, H. Yoo, and D. Gweon, "Chromatic confocal microscopy with a novel wavelength detection method using transmittance," *Opt. express* **21**, 6286–6294 (2013).
23. J. Schlarp, E. Csencsics, and G. Schitter, "Design and evaluation of an integrated scanning laser triangulation sensor," *Mechatronics* **72**, 102453 (2020).
24. G. Berkovic and E. Shafir, "Optical methods for distance and displacement measurements," *Adv. Opt. Photon.* **4**, 441–471 (2012).
25. A. Streicher, "spectra-cular" measurements," *Optik & Photonik* **12**, 38–40 (2017).
26. P. J. Besl and N. D. McKay, "Method for registration of 3-d shapes," in *Sensor fusion IV: control paradigms and data structures*, vol. 1611 (International Society for Optics and Photonics, 1992), pp. 586–606.
27. Microepsilon, *confocalDT // Confocal chromatic sensor system* (2021). Retrieved from <https://www.micro-epsilon.com/download/products/cat--confocalDT--en.pdf>.
28. E. Csencsics, J. Schlarp, T. Schopf, and G. Schitter, "Compact high performance hybrid reluctance actuated fast steering mirror system," *Mechatronics* **62**, 102251 (2019).
29. J. Wang, G. Zhang, and Z. You, "Design rules for dense and rapid lissajous scanning," *Microsystems & Nanoeng.* **6**, 1–7 (2020).

Post-print version of the article: D. Wertjanz, T. Kern, E. Csencsics, G. Stadler, and G. Schitter, "Compact scanning confocal chromatic sensor enabling precision 3-D measurements," *OSA - Applied Optics* Vol. 60, Issue 25, pp. 7511-7517, 2021. DOI: [10.1364/AO.428374](https://doi.org/10.1364/AO.428374)

© 2021 Optical Society of America. One print or electronic copy may be made for personal use only. Systematic reproduction and distribution, duplication of any material in this paper for a fee or for commercial purposes, or modifications of the content of this paper are prohibited.